Particle Image Velocimetry Experiment Analysis Using Large-Eddy Simulation: Application to Plasma Actuators

F. Laurendeau, O. Leon, F. Chedevergne, J.M. Senoner, G. Casalis

Particle Image Velocimetry Experiment Analysis Using Large-Eddy Simulation: Application to Plasma Actuators

F. Laurendeau,* O. Léon,† F. Chedevergne,‡ J.-M. Senoner,* and G. Casalis*
ONERA—The French Aerospace Lab, 31055 Toulouse, France

DOI: 10.2514/1.J055687

This article presents an analysis of a planar particle image velocimetry experiment aiming at measuring the phase-averaged velocity fields of a synthetic jet generated by a plasma synthetic jet actuator. Three major sources of uncertainty related to this type of experiment are examined: the phase-averaging process, the estimation of the vertical position of the wall into which the actuator is inserted, and the position of the laser sheet plane. Furthermore, the present work investigates the errors related to the dynamics of the particles used for seeding this type of high-speed transient flow. As expected, uncertainties associated with the phase-averaging process and the estimation of the wall position may be directly estimated from the measurements. However, estimation of the uncertainties originating from the position of the laser sheet plane and the errors related to the particle dynamics require additional information. In the present work, an original methodology relying on a numerical model of the actuator is thus proposed. This model, based on a large-eddy simulation, is able to reproduce the main features of the jet observed in the experiments and is used to generate realistic synthetic particle images. The influence of the laser sheet position on the velocity uncertainties and the errors associated with the particle dynamics are then explored. Experimental and numerical findings are considered to conclude in a quantitative manner on the dominant sources of uncertainty for such experiments and on the errors induced by particle dynamics that should be expected.

Nomenclature

C	=	global concentration of particles at the initial instant
C_d	=	capacitance of the discharge circuit
d	=	particle class diameter
d_d	=	diffraction limited minimum image diameter
d_p	=	particle diameter
d_τ	=	particle image diameter
$F(d)$	=	occurrence probability of the class diameter d
I	=	discharge current
j	=	imaginary unit
M	=	magnification factor of the lens
$\boldsymbol{m}$	=	pixel identifier
N	=	number of measurement points
n_m	=	number of instantaneous images used in the averaging process
R	=	orifice radius
Re_p	=	particle Reynolds number
r	=	distance between the laser sheet and actuator orifice
St	=	Stokes number
t	=	time variable
t_b	=	breakdown instant
t_{LES}	=	instant extracted from the simulation
U	=	horizontal velocity
U_b	=	breakdown voltage
U_c	=	voltage across the capacitor
$u_{\mathrm{ave}}(\boldsymbol{m})$	=	standard uncertainty due to the phase-averaging process
u_h	=	standard uncertainty of the wall vertical position
$u_r(\boldsymbol{m})$	=	standard uncertainty due to the uncertainty of the laser sheet position
$u_{y_0}(\boldsymbol{m})$	=	standard uncertainty due to the uncertainty of the wall vertical position
V	=	vertical velocity
$\mathcal{V}_{\mathrm{cell}}$	=	volume of the initial cell
$\boldsymbol{V}_g$	=	gas velocity vector at the particle location
V_g	=	monodimensional gas velocities at the particle location
$\hat{V}_g$	=	complex amplitude of the monodimensional gas velocity at the particle location
$V^i(\boldsymbol{m})$	=	instantaneous vertical velocity
$\bar{V}(\boldsymbol{m})$	=	phase-averaged vertical velocity
$V_{\max}$	=	maximal velocity of the flow
$\boldsymbol{V}_p$	=	particle velocity vector
V_p	=	monodimensional particle velocities
$\hat{V}_p$	=	complex amplitude of the monodimensional particle velocity
y_0	=	wall vertical position
Δt_{jet}	=	duration between electrical breakdown and particle image velocimetry measurement
$\tilde{\Delta} t_{\mathrm{jet}}$	=	effective measurement instant
μ_g	=	gas viscosity
ρ_p	=	particle density
σ_m	=	experimental standard deviation of the velocity
τ_g	=	characteristic timescale of the flow
τ_p	=	particle relaxation time
ω_g	=	oscillation frequency of the freestream

Received 19 September 2016; revision received 13 April 2017; accepted for publication 31 May 2017; published online 27 July 2017.

*Department of Aerodynamics and Energetics Modeling.
†olivier.leon@onera.fr (Corresponding Author).
‡francois.chedevergne@onera.fr (Corresponding Author).

I. Introduction

A. Plasma Synthetic Jet Actuator

In THE past decades, synthetic jets have been studied both experimentally and numerically to efficiently control the dynamics of various wall-bounded and free shear flows. Compared with continuous or pulsed jets, a considerable advantage of this flow-control technology lies in a zero-net mass-flux over an actuation cycle. As reviewed by Cattafesta and Sheplak [1], synthetic jets are commonly generated by actuators designed with a piezoelectric diaphragm, an electrodynamic diaphragm, or a piston. These actuation systems have proved their efficiency in various aerodynamic configurations, as reviewed for example by Glezer [2] and Glezer and Amitay [3].

However, the velocity of the jets generated by such systems does not usually exceed 100 $\mathrm{m} \cdot \mathrm{s}^{-1}$. The velocity ratio of these jets to the upstream flow being a key parameter, this appears insufficient for the efficient control of high-speed flow cases. Since 2003, the Applied Physics Laboratory at Johns Hopkins University has developed a device named the SparkJet actuator [4], which is able to generate synthetic jets with velocities up to about 500 $\mathrm{m} \cdot \mathrm{s}^{-1}$. To contribute to

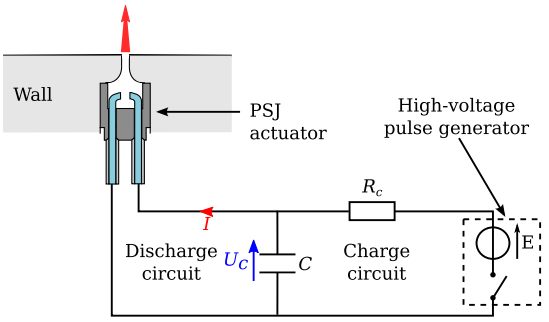

Fig. 1 Diagram of the PSJ actuator inserted into a wall, defining the boundary of a flow, and its electric power supply.

these research efforts, ONERA, in collaboration with the Centre National de la Recherche Scientifique LAPLACE laboratory, has been working on a similar actuator concept referred to as the plasma synthetic jet (PSJ) actuator.

A schematic of the PSJ actuator and its electric power supply is provided in Fig. 1. The actuator is mounted into a wall, usually defining the boundary of an external flow. It is designed with two electrodes located in a cavity, the latter being opened to the external flow through a convergent nozzle with an exit radius $R = 0.5$ mm. The two electrodes are connected to a capacitor C_d and energy is supplied by a high-voltage pulse generator.

The PSJ actuator operating cycle can be sequenced in three successive phases. At the beginning of a cycle, the high-voltage switch is closed and the capacitor charges until the voltage between the electrodes reaches the breakdown voltage of the surrounding air, initiating an electric arc. The arc discharge between the electrodes is then sustained by the capacitor, which typically lasts 5 μs. From an aerodynamic point of view, this electrical process corresponds to the energy deposition phase. Temperature and pressure in the cavity increase up to about several tens of thousands Kelvin and several bar, respectively. This leads to the generation of a jet at the exhaust orifice, yielding the ejection phase. The jet typically develops over a length of $10R$ in a quiescent environment and lasts about 100 μs. Its topology is composed of a train of successive vortex rings being advected with different velocities, potentially leading to vortex pairing. Finally, driven by simple pressure recovery in the cavity, a natural suction phase occurs, allowing the PSJ actuator to perform another cycle. Typically, this phase lasts several times the ejection duration, for low-frequency actuation.

This type of actuation device has already been employed for active control of various aerodynamic configurations in the literature [5–10]. Building upon these successful application cases, an incremental step necessary to efficiently leverage the PSJ actuator for future applications is to precisely characterize and understand the generation and the development of the jet. Bearing this objective in mind, this paper presents a primary study aiming at measuring the velocity field of the jet generated by the actuator without any external flow using particle image velocimetry (PIV). The experimental technique employed is derived from the work of Reedy et al. [11], Ko et al. [12], and Cybyk et al. [13] and consists of placing the actuator into a chamber seeded with tracer particles. The latter are assumed in suspension at the beginning of each actuation cycle and dragged as the jet is developing in a quiescent environment. The main objective of the present article is to examine two fundamental aspects of this type of planar PIV experiment: the uncertainty of the phase-averaged velocity fields obtained using such a technique on millimeter-scale jets with strong velocity gradients and the dynamics of the particles employed as tracers for PIV measurements in such high-speed transient flows.

B. Uncertainty Analysis

First of all, for such PIV experiments, various sources of measurement uncertainties have to be taken into account. In a general manner, these uncertainties are typically arising from the measurement system itself, through temporal or spatial calibration uncertainties, for example, from the postprocessing of the PIV images [14], from the estimation of the flow statistics, etc. In the present case of study, three main sources of uncertainty are considered in the evaluation of phase-averaged velocity fields obtained with this type of actuator: the velocity dispersion of the phase-averaged fields, the estimation of the vertical location of the wall, and the position of the PIV laser sheet plane. These last two sources of uncertainties appear to be important for such studies due to the millimeter scale of the flow induced by the actuator, which can be challenging for accurate planar PIV measurements. In the literature dealing with planar PIV measurements on such flows, these technical points to keep in mind while analyzing the results are rarely addressed. For example, in the work of Reedy et al. [11], an uncertainty analysis was performed based on the methodology proposed by Lazar et al. [15], thus accounting for many sources of uncertainty but not highlighting the importance of the two previous ones. In a more recent work, Zong and Kotsonis [16] acknowledge such sources of uncertainty while performing PIV measurement on a PSJ actuator and provide a simple way to approximately estimate the uncertainty associated with the laser sheet thickness. Because such PIV measurements are performed in a single plane and with a single laser sheet thickness, such uncertainty estimates cannot be obtained by solely relying on the measured velocity fields. These authors then based their uncertainty estimation on a very simplified parabolic representation of the jet. The present study aims at providing further insight in such uncertainty estimation process by relying on a more representative model of the flow of interest. This is particularly important to address the uncertainty estimation of PIV measurements performed in a longitudinal plane of a given thickness that might not be perfectly centered on the jet axis, as observed in the present experiment reported in Sec. II.

C. Particle Dynamics

Second, a thorough characterization of particle dynamics is necessary for such high-speed transient flows to guarantee that the velocity field measured with PIV is sufficiently close to the actual gaseous flowfield. This is also scarcely considered in the literature for the present type of flows, despite its significance as explained in the following.

Under the classical assumptions made for PIV experiments in gases [17,18], that is, sufficiently small particle diameter and high density ratio between particle and gas, the dominant force governing the particle's motion is drag. The particle's equation of motion then writes

$$\frac{\mathrm{d}\boldsymbol{V}_p}{\mathrm{d}t} = -\frac{1}{\tau_p}(\boldsymbol{V}_p - \boldsymbol{V}_g) \tag{1}$$

where $\boldsymbol{V}_p$ is the particle velocity vector at instant t, $\boldsymbol{V}_g$ is the gas velocity vector at the particle location at instant t, and τ_p is the particle relaxation time. Considering the flowfield to be dominated by viscous effects at the particle scale, the particle relaxation time reduces to

$$\tau_p = \frac{d_p^2 \rho_p}{18\mu_g} \tag{2}$$

Particle trajectories will coincide with those of fluid elements as the Stokes number St, which is defined as the ratio of the particle relaxation time τ_p to the characteristic timescale of the flowfield τ_g, tends toward zero. A simple way to illustrate particle dynamics consists of calculating a particle's response to a sinusoidal oscillation of the freestream in a monodimensional framework [18,19]. The transfer function reads

$$\frac{\hat{V}_p}{\hat{V}_g} = \frac{1}{1 + j\omega_g \tau_p} = \frac{1}{1 + jSt} \tag{3}$$

where $V_p = \hat{V}_p e^{j\omega_g t}$ and $V_g = \hat{V}_g e^{j\omega_g t}$ with j as the imaginary unit and ω_g as the oscillation frequency of the freestream. V_p and V_g are,

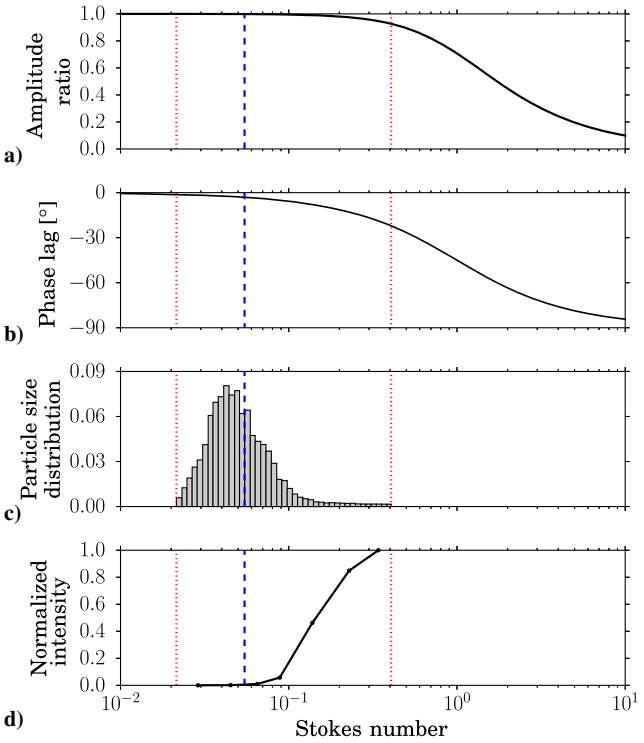

Fig. 2 As a function of the Stokes number: a) amplitude ratio, b) phase lag between freestream and particle velocities, c) experimental particle size distribution, and d) normalized intensity scattered by particles to the camera.

respectively, the monodimensional particle and gas velocities at the particle location. The modulus and argument of this transfer function, represented in Figs. 2a and 2b, respectively, correspond to the amplitude ratio and the phase lag of the particle velocity compared with the gas velocity, as a function of the Stokes number. In these figures, Stokes number bounds evaluated with the extremum diameters of the particle size distribution of the present experiment are indicated by dotted red lines, whereas the Stokes number based on the mean particle diameter is represented by a dashed blue line. These Stokes number values, ranging from 0.02 to 0.4, are comparable to those reported by Reedy et al. [11,20] and they are, in all likelihood, lower than those encountered by Ko et al. [12] and Cybyk et al. [13]. In many reports of PIV experiments, evaluations of Stokes numbers are solely based on a mean particle diameter. In the present experiment, such a Stokes number provides an amplitude ratio greater than 99% and a phase lag of about −3 deg, values that are fully appropriate for a PIV experiment. However, using a Stokes number based on the maximum diameter of the particle size distribution, the amplitude ratio approaches 0.9 and the phase lag is approximately −20 deg. The ability of the particles to perfectly follow the gas flow is thus not established if the overall particle diameter distribution is considered. In addition, as previously mentioned, an estimation of the characteristic time of the flow dynamics is required to evaluate a Stokes number. Here, this characteristic time is evaluated such that $\tau_g = R/V_{\max}$ where $V_{\max} \approx 200\ \mathrm{m \cdot s^{-1}}$ is an overestimation of the maximal velocity reached in the jet. There is no evidence that this characteristic time applies to the entire jet dynamics. Finally, the analysis of the transfer function as provided by Eq. (3) is only fully appropriate for a steady-state situation. In the current experiment, the particles are initially in suspension, with a velocity close to zero, and experience a transient increase in velocity as the jet develops. Compared with the steady-state case, this transient phase may induce significantly higher velocity differences between the particles and the gas. Figs. 2c and 2d, respectively, depict the particle size distribution expected in the current experiment and the normalized light intensity scattered by the seeding particles to the camera, as a function of the Stokes number. As observed in these figures, the concentration of large particles is much lower than the one of median particles, whereas the formers scatter much more light toward the camera. Yet, in PIV algorithms, velocity fields are evaluated through correlations between two consecutive image intensity functions. The high intensity scattered by the largest particles therefore tends to bias the correlation toward their velocities, whereas their low concentration plays the opposite role. Therefore, it appears necessary to determine whether the largest particles induce significant errors in the velocity reconstruction or not.

In the literature, several authors have already tackled such particle dynamics issues with a focus on PIV measurements. Samimy and Lele [21] conducted the direct numerical simulation (DNS) of a two-dimensional compressible free shear layer with particles of different diameters to determine their respective trajectories. They showed that only particles with $St < 0.05$ were able to follow fluid particle trajectories in zones of high vorticity. Williams et al. [22] examined particle dynamics in a supersonic flow with an oblique shock and compared their results with PIV measurements. Mitchell et al. [23] calculated the trajectories of particles passing through a normal shock. Providing some strong assumptions, these authors reformulated a PIV correlation function to make it only dependent on the particle diameters and positions. Thereby, they showed that the velocities evaluated using the simplified PIV algorithm was significantly dependent on the particle distributions. Finally, de Silva et al. [24] generated numerical particle images, assuming that these particles followed a channel flow simulated by DNS. With these images, they simulated a tomographic PIV experiment to investigate the influence of some experimental parameters, such as the camera position or the spatial resolution.

D. Contributions

This article combines these numerical approaches to study the PIV measurement uncertainties previously identified and the errors induced by nonideal seeding particle dynamics for the present type of flows. First of all, the PIV measurements of the jet generated by the PSJ actuator are presented in Sec. II. Estimates of the measurement uncertainties that may directly be obtained from the experiments are then provided. Second, a numerical model of the experiment is developed to analyze the uncertainties and errors that cannot be solely characterized relying on the measurements. Section III thus presents a large-eddy simulation (LES) model that reproduces the main flow features of the jet generated by the actuator and compares its results with the PIV measurements. This simulation is then employed to emphasize the significance of the laser sheet position uncertainty on the measured velocity. Finally, in Sec. IV, the trajectories of synthetic seeding particles are computed using this LES, and numerical particle images are generated and postprocessed using the same PIV algorithm as in the experiment. Comparisons of the synthetic PIV results with the exact gaseous velocity fields of the LES provide an estimate of the measurement errors to expect in such flows due to the particle dynamics.

II. PIV Measurements of the Jet Generated by the PSJ Actuator

A. Experimental Setup

The PSJ actuator is tested in a quiescent environment, with the actuation frequency set to 1 Hz. Considering the characteristic timescales of the PSJ actuator previously mentioned, it can be assumed as working in a single-pulse mode. Two types of measurements are performed. First, a planar two-dimensional two-component PIV setup is employed to measure the jet velocity fields in a longitudinal plane. Because of the short duration of the jet development, only one PIV image pair can be acquired during an operating cycle of the actuator. This acquisition is repeated over 500 cycles for each selected instant covering the jet development to perform phase-averaged measurements. Second, electrical signals are measured together with each acquisition of a PIV image pair. These signals provide a characterization of the discharge; they also allow identification of the key instants of the experiment: the breakdown instant and the instants when the laser pulses are

generated. With these data, a very precise evaluation of the synchronization of the PIV acquisitions relative to the breakdown instants can be obtained for every set of 500 measurements.

1. *PIV Setup*

The actuator compactness prevents a direct seeding of the cavity. Therefore, the ambient air in which the jet develops is seeded instead. This indirect seeding approach has been previously successfully employed for this type of actuator [11–13] and for other types of actuators generating synthetic jets [25–27]. The PSJ actuator is mounted normal to the floor of a closed airtight chamber, depicted in Fig. 3, where seeding particles are introduced. The size of the chamber appears sufficiently large to assume that the jet develops in a semi-infinite environment. Furthermore, particle images show that the seeding of the environment is homogeneous and that the particles have a negligible velocity at the beginning of each actuation. Thus, the environment can be considered quiescent and the particles at rest at the beginning of each cycle.

Seeding particles are obtained using a Topas ATM 210 atomizer supplied with Di-Ethyl-Hexyl-Sebacat (DEHS). The particle size distribution provided by the manufacturer is displayed in Fig. 2c. Although this distribution may have been modified through the piping and the chamber, there is no straightforward manner to estimate the resulting distribution. Therefore, the particle size distribution provided by the manufacturer is directly used to model the polydispersion of the seeding particles in the region where the jet develops. The mean diameter of this distribution is 0.22 μm.

A system from LaVision is employed for the PIV measurements. The laser light sheet is generated by a double-pulse neodymium yttrium aluminum garnet laser from Quantel (Twins BSL), delivering about 150 mJ per pulse at a wavelength of 532 nm. This laser sheet is oriented normal to the floor of the chamber, so as to intersect the actuator orifice, and defines the x–y plane of measurement, with the x axis oriented along the floor and the y axis normal to the floor. To limit laser light reflections to the camera, a coating of Rhodamine 6G is applied on a layer of black paint on the floor of the chamber, where the actuator is inserted. The position of the laser sheet is evaluated at the end of the experiment by simply looking at the mark left by the laser light sheet on the Rhodamine coating: The distance between the center of the actuator circular exhaust orifice and the center of the laser sheet is found to be $r = 0.25 \pm 0.1$ mm. The width of the laser light sheet at the measurement location is determined using a DataRay WinCamD laser beam analyzer, yielding an estimated value of 0.38 mm. PIV image pairs are acquired with a LaVision Imager Pro X camera, offering a resolution of 2048×2048 pixels, with a pixel size of 7×7 μm, on which a Sigma 180 mm macrolens is mounted. An optical calibration of the system is performed with a dedicated reference body and yields a maximum standard error of about 0.4 pixels. With this setup, the visualization zone has dimensions of about 20×20 mm.

Finally, it is assumed that the phase-averaged jet generated by the actuator is axisymmetric. This assumption might not seem straightforward owing to the presence of the two electrodes in the cavity (see Figs. 1 and 3). However, three-dimensional simulations performed by Laurendeau et al. [28] showed that these electrodes have only a very limited influence on the symmetry of the jet. Consequently, the angular orientation of the laser light sheet relative to the plane containing the two electrodes is not considered in the present experiment. The symmetry of the jet in the measurement plane will be verified in Sec. III.

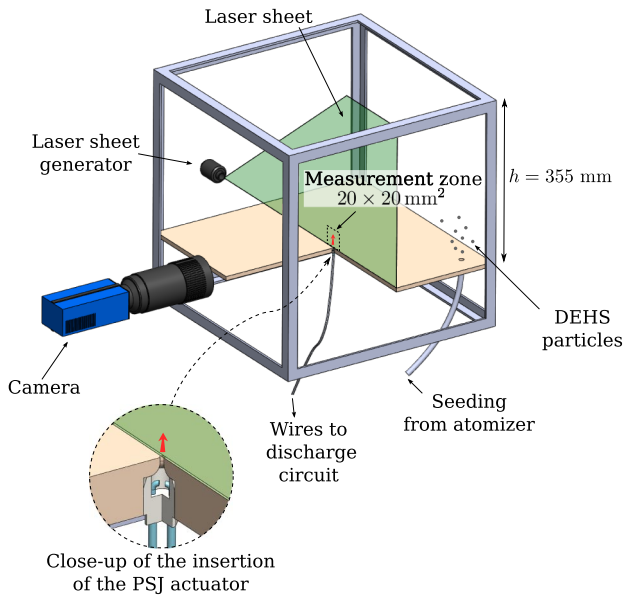

Fig. 3 Diagram illustrating the planar PIV setup and the flow visualization chamber; a quarter of the floor in which the PSJ actuator is inserted was removed for clarity.

2. *Electrical Setup*

The measured electrical signals are the voltage across the capacitor U_c, the current in the discharge circuit I, and the Q-switch output signal of the first laser head. A high-voltage probe Elditest GE.3830 presenting a limited bandwidth of 3 MHz is employed to measure U_c. The intensity I is measured using a Magnelab CT-D0.5 current probe, offering a higher bandwidth of 200 MHz. All of these signals are recorded on a computer at each actuation cycle.

B. Electrical Analysis

1. *PIV Images Selection*

Figure 4 shows a histogram of the duration between the electrical breakdown and the PIV measurement, noted Δt_{jet}, for a typical set of 500 measurements at a particular phase of the jet development. These data are deduced from the electrical measurements. The temporal dispersion of the measurements is because the PIV system could not be directly synchronized with the breakdown voltage. To limit the statistical uncertainty on the velocity fields induced by this temporal dispersion, a selection is performed among the PIV images. A selection window with a width of 2 μs is applied (see Fig. 4). It is centered to maximize the number of selected image pairs. The distribution of Δt_{jet} within the selection window is often close to a Gaussian distribution. The window center is then defined as the effective measurement instant and is denoted $\tilde{\Delta} t_{\text{jet}}$. A similar selection process is applied to the breakdown voltage value to limit the dispersion of the velocity measurements due to its variation. The size of the selection window is 150 V.

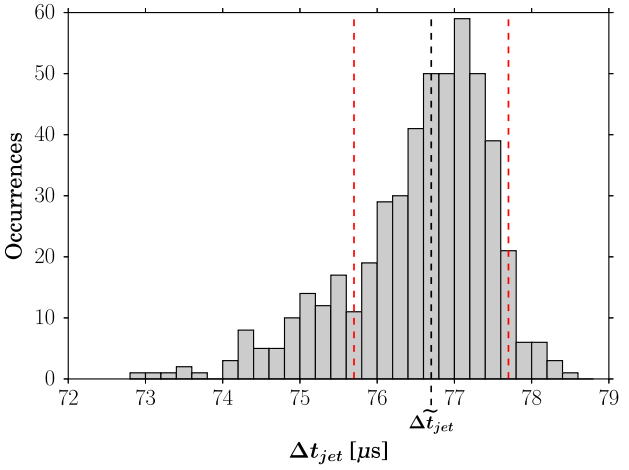

Fig. 4 Histogram of PIV measurement instants in the jet development Δt_{jet} relative to the breakdown instant t_b. The result of the PIV images selection process is represented by vertical dashed lines: the effective measurement instant $\tilde{\Delta} t_{\text{jet}}$ is indicated by the black line, and the bounds of the temporal window ($\tilde{\Delta} t_{\text{jet}} \pm 1$ μs) are depicted by the red lines.

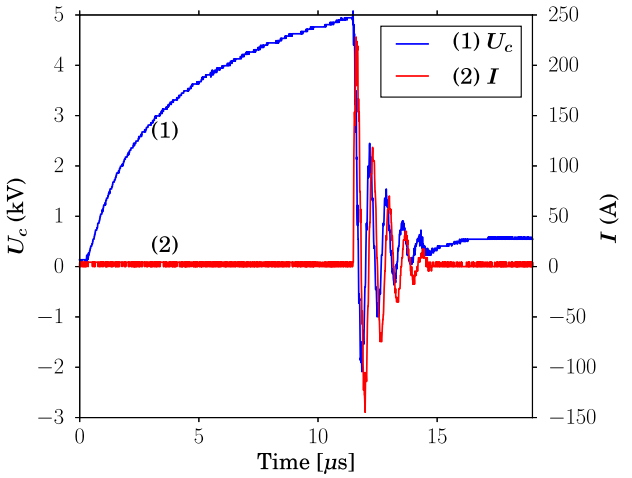

Fig. 5 Capacitor voltage U_c and current in the discharge circuit I (see Fig. 1) measured during one PSJ actuation cycle.

2. Characterization of the Discharge

Typical measurements of the voltage across the capacitor U_c and the discharge current I during one actuation cycle are plotted in Fig. 5. It is important to notice that these signals are acquired together with a PIV acquisition, thus with seeding particles inevitably present in the cavity of the actuator. Nonetheless, these measurements are very similar to the ones obtained without seeding, suggesting that the particles present in the cavity of the actuator do not interfere significantly with the electrical process. At the beginning of the actuation cycle, shortly after $t = 0$ μs, the evolution of the voltage across the capacitor matches the expected charging of a resistor–capacitor series circuit, previously described in Fig. 1. The discharge circuit being open, the current is null. At about $t = 11.5$ μs, as the voltage across the capacitor U_c reaches the breakdown voltage value of air U_b, an electrical breakdown occurs. At this moment, the plasma generated between the electrodes closes the discharge circuit: U_c and I then describe underdamped oscillatory responses, which is characteristic of a spark-type discharge [29,30].

These measured signals, once averaged and fitted with a resistor–inductor–capacitor model, following Belinger et al. [31] and Greason [30], are used in the following LES model of the actuator in Sec. III as an input.

C. Velocity Fields

An example of a particle image acquired during the experiment is provided in Fig. 6. In this image, the wall containing the actuator is located at the bottom and is identified using the laser reflections. The particle concentration appears very heterogeneous but allows identification of the key characteristics of the jet topology. The boundaries of the flow are well seeded with particles that are pushed by the forming jet. As expected, the high-vorticity zones of the flow (i.e., the cores of the vortex rings generated by the jet) are poorly seeded and yield the darkest areas. This is because a vortex ring is a recirculation zone where particles having a low Stokes number, and thus accurately following the flow, cannot enter. Furthermore, particles initially present inside a vortex ring are likely to be ejected from the latter [21]. On the other hand, the jet core appears sufficiently seeded. The particles may come from the surroundings of the jet and may have been dragged by vortex rings to the jet core. They may also come from the cavity because some particles may have been drawn in during the previous recovery phase, as later discussed in Sec. IV.

From these observations, it appears that instantaneous velocity fields cannot be relevantly calculated in some areas of such instantaneous PIV images due to insufficient local seeding. These areas are mainly located around the vortex cores. However, their locations randomly vary from an image pair to another. By combining a whole set of image pairs selected by the previous electrical analysis, complete phase-averaged fields can be obtained

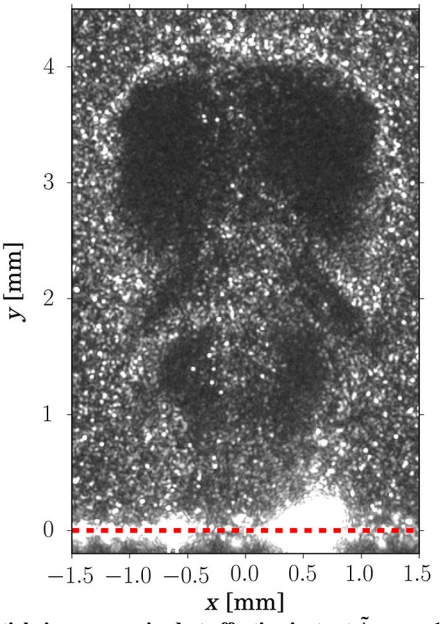

Fig. 6 Particle image acquired at effective instant $\tilde{\Delta}t_{\text{jet}} = 115$ μs. The brightness has been artificially increased for the sake of clarity; nonetheless, the particles and the usable texture in the vortex cores may not be distinguishable on a print. The red dashed line displays the estimated wall position.

with a sufficient number of samples per window to provide relevant mean values.

All velocity fields were computed using the ONERA in-house software FOLKI-SPIV [32], based on an iterative Lucas–Kanade algorithm. This algorithm performs precise and fast computations of dense PIV vector fields through graphics processing unit implementation. As in more traditional PIV software, the algorithm acts on the velocity field as a moving average, with the width being driven by the size of the interrogation windows. For the present experiment, interrogation windows with a size of 31×31 pixels, representing a zone of 0.309×0.309 mm, were employed. Interrogation windows displaying insufficient seeding were discarded from the calculation by applying a minimum threshold of 1% on the texture, defined as the standard deviation of the intensity. Furthermore, only interrogation windows presenting correlation scores greater than 30% were used in the phase-averaging process. Finally, a background image subtraction and a mask applied near the floor were used to limit the impact of laser reflections on the calculation of vector fields.

D. Uncertainty Estimates from PIV Measurements

Some measurement uncertainties can be directly evaluated from such PIV results. First, the velocity dispersion observed while averaging the instantaneous velocity fields measured by PIV is considered. This source of uncertainty intrinsically accounts for several distinct phenomena: the statistical dispersion of Δt_{jet} and current intensity I, turbulence of the flow, initial distributions of the seeding particles, error induced by local transverse velocities, inaccuracies of the PIV algorithm itself in the evaluation of instantaneous velocity fields [14], etc. For each interrogation window, the standard uncertainty of the vertical phase-averaged velocity resulting from the phase-averaging process may be expressed as

$$u_{\text{ave}}(\boldsymbol{m}) = \frac{\sigma_m}{\sqrt{n_m}}, \quad \text{with} \quad \sigma_m = \sqrt{\frac{1}{n_m - 1}\sum_{i=1}^{n_m}[V^i(\boldsymbol{m}) - \bar{V}(\boldsymbol{m})]^2} \tag{4}$$

where n_m is the number of instantaneous images used in the averaging process at the pixel $\boldsymbol{m}$, σ_m is the experimental standard

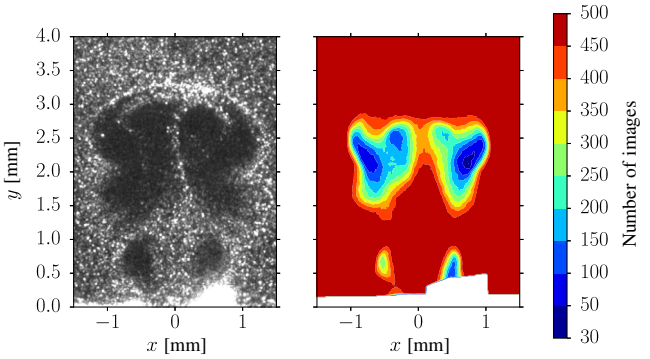

Fig. 7 Particle image obtained at an effective instant $\tilde{\Delta}t_{\text{jet}} = 94.6\ \mu$s (left image) together with the contour map of number of images used in each PIV interrogation window for the phase-averaging process at the same effective instant (right image).

deviation of the velocity, $V^i(\boldsymbol{m})$ are the measured instantaneous velocities, and $\bar{V}(\boldsymbol{m})$ is the phase-averaged velocity. As indicated in Sec. II.C, interrogation windows displaying insufficient texture or correlation are discarded from the averaging process. Figure 7 provides the number of instantaneous images used in the averaging process for the effective measurement instant $\tilde{\Delta}t_{\text{jet}} = 94.6\ \mu$s. An example of particle image obtained at this instant is also given. It appears that the areas displaying the lowest number of images used in the averaging process correspond to the location of the leading vortex ring, which can be related to poor particle seeding in this area. The mask effect is also clearly visible at the bottom of Fig. 7. Relative velocity uncertainties can be defined by dividing the uncertainty results u_{ave} by the maximum vertical velocity V_{max} of the current phase-averaged field. The resulting fields are gathered in Fig. 8. As observed in Fig. 8a, this source of uncertainty yields maximum relative velocity uncertainties of about 1.5–2% in very localized regions of the jet, where seeding is the lowest, in agreement with Fig. 7.

A second source of uncertainty lies in the estimation of the vertical position of the wall on the images. The standard uncertainty associated with this identification process reads

$$u_{y_0}(\boldsymbol{m}) = \frac{\partial \bar{V}(\boldsymbol{m})}{\partial y_0} u_h \tag{5}$$

where $\partial \bar{V}(\boldsymbol{m})/\partial y_0$ is the partial derivative of the phase-averaged velocity with respect to the wall position y_0, expressed in pixel, and u_h is the standard uncertainty of the wall position. The term $\partial \bar{V}(\boldsymbol{m})/\partial y_0$ is estimated through second-order central finite difference and the term u_h is evaluated from the laser light reflections observed in the PIV images. The height of these reflections is lower than $h = 6$ pixels and the standard uncertainty is thus

$$u_h = \frac{h}{2\sqrt{3}} \tag{6}$$

which is the standard deviation of a rectangular distribution with a width h. Here again, relative uncertainties are defined with respect to the maximum velocity V_{max}. As observed in Fig. 8b, the resulting relative velocity uncertainty appears moderate and very localized, with a maximum value hardly exceeding 2.5%. Values of about 1–2% are mainly found around the leading vortex due to velocity gradients in the vertical direction.

These results show that the orders of magnitude of the relative velocity uncertainties deduced from the measurements are moderate, with typical local values found around 1.5% in regions close to the leading vortex. Assuming these sources of uncertainty uncorrelated, one could derive a global uncertainty estimate from such results, relying on the propagation of uncertainties [33]. However, it is emphasized that some sources of uncertainty that can be of significance for the present study, where millimeter-scale planar PIV measurements are performed, are not taken into account in the present discussion. Particularly, in this experiment, the exact location of the PIV plane of measurement relative to the actuator orifice presents an uncertainty, as highlighted in Sec. I, such that $r = 0.25 \pm 0.1$ mm, which is difficult to reduce due to the scales of the system. Because of the large velocity gradients of the flow considered, this slight location uncertainty may induce large velocity uncertainties. Furthermore, such a velocity uncertainty cannot be directly evaluated from the measurements because the laser sheet position is fixed in the experiment. The numerical model of the PSJ actuator presented in the following section will then be employed to explore this point and to emphasize the importance of accounting for such a source of uncertainty, which should be acknowledged when analyzing such measurements.

III. LES Model of the PSJ Actuator

As emphasized in the previous sections, the PIV measurements obtained cannot allow to conclude on two points: the significance of the uncertainty associated with the laser sheet location and the significance of the particle dynamics errors. The following sections

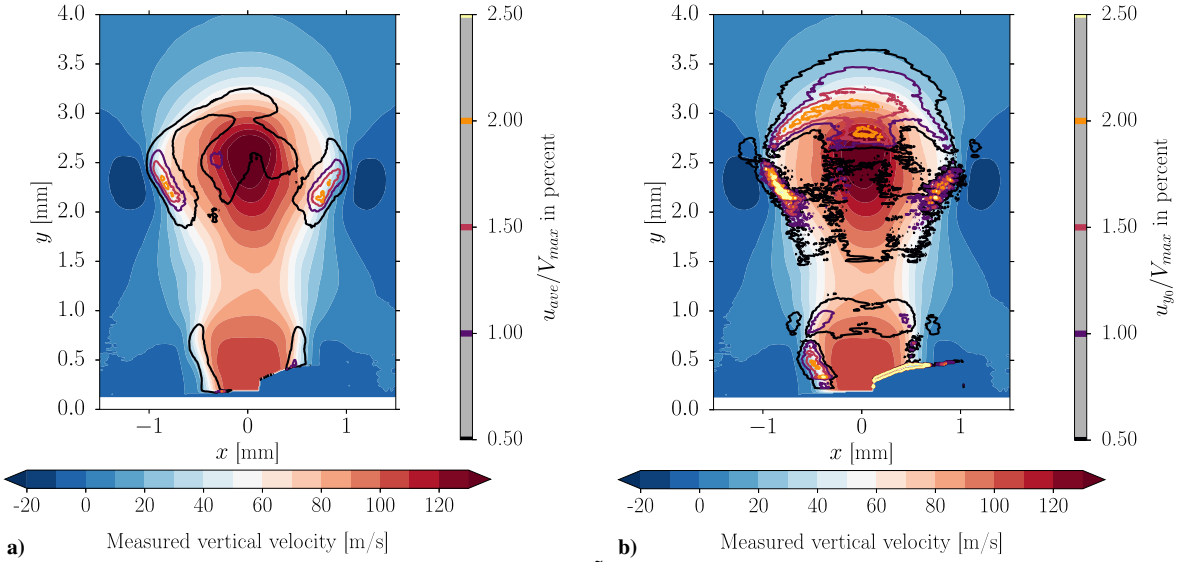

Fig. 8 Phase-averaged experimental vertical velocity field $\bar{V}$ at the instant $\tilde{\Delta}t_{\text{jet}} = 94.6\ \mu$s overlaid with isolines of relative velocity uncertainty due to a) the phase-averaging process ($u_{\text{ave}}/V_{\text{max}}$) and b) the estimation of the vertical position of the wall y_0 (u_{y_0}/V_{max}).

of the article intend to address these points by relying on a numerical model of the actuator.

A. Numerical Setup and Postprocessing

The model from Laurendeau et al. [28] is used because it is able to reproduce the features of the jet observed in a schlieren experiment. This model is based on an LES of the actuator and the environment where the jet develops. Numerical parameters are similar to those presented by Laurendeau et al. [28]. In the present study, an unstructured mesh composed of about six million cells has been used. The energy deposited by the plasma into the cavity via Joule effect is taken into account through energy source terms. The calculation of these source terms is based on the following main assumptions.

Following the work of Belinger et al. [31], the plasma is assumed at local thermal equilibrium. The electric field between the electrodes is supposed oriented in the interelectrodes direction. It can vary in this direction only and is time dependent. In addition, the discharge channel boundaries are determined using a threshold on the temperature. The model was slightly improved with respect to the description given by Laurendeau et al. [28]. Presently, the calculation of the source terms, representing the energy deposition, is carried out together with the LES, both computed with the ONERA in-house computational fluid dynamics (CFD) code CEDRE. To avoid modeling the electrical circuit, a signal of current intensity is directly used in the LES.

To compare the simulation results with experimental data, the LES velocity fields are postprocessed following two additional steps. The objective is to account for the laser sheet width and the PIV interrogation window size in the PIV measurement process, which are, respectively, $0.76R$ and $0.62R$, with R being the actuator orifice radius. Indeed, these values are clearly far from negligible with respect to the characteristic flow length scales. First, the data contained in a slice representative of the experimental laser sheet are extracted from the simulation results. These data are then averaged over the width of the slice, using weights following a Gaussian distribution similar to the light intensity distribution found over the laser sheet width. Afterward, these two-dimensional data are interpolated on a grid equivalent to the one observed by the PIV camera sensor in the object plane. A moving average is then applied to these data, with a width equal to the PIV interrogation windows size. As performed by FOLKI-SPIV software, an interrogation window is computed around each pixel. This process will be referred to as the PIV-like process in the following.

B. Comparison with PIV Measurements

The experimentally measured phase-averaged velocity fields are here compared with the LES results. The effective measurement instant $\tilde{\Delta}t_{\text{jet}} = 94.6\ \mu$s is particularly analyzed in detail because it appears sufficiently representative of the entire measurement set.

Figures 9 and 10 show the phase-averaged velocity fields measured by PIV and the velocity fields obtained with the model and

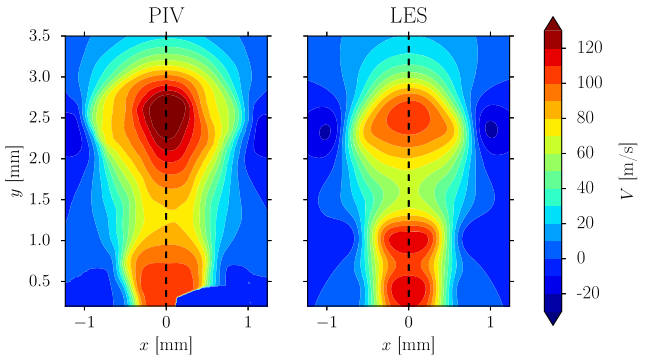

Fig. 9 Comparison of vertical velocity fields between the phase-averaged PIV results $\bar{V}$ obtained at the effective instant $\tilde{\Delta}t_{\text{jet}} = 94.6\ \mu$s and the LES velocity field V calculated at the instant $t_{\text{LES}} = 94\ \mu$s.

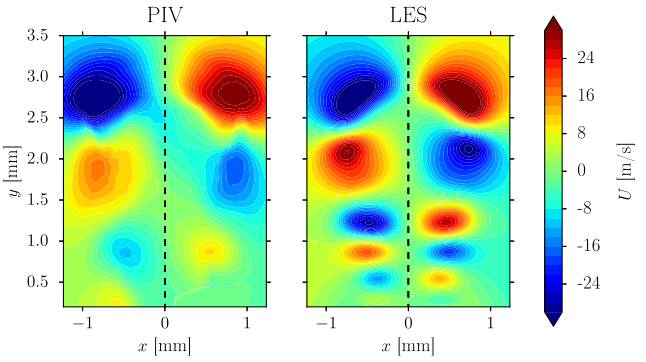

Fig. 10 Comparison of horizontal velocity fields between the phase-averaged PIV results $\bar{U}$ obtained at the effective instant $\tilde{\Delta}t_{\text{jet}} = 94.6\ \mu$s and the LES velocity field U calculated at the instant $t_{\text{LES}} = 94\ \mu$s.

processed as previously explained. The vertical velocity is referred to as V and the horizontal one is written as U.

The jet is composed of several vortex rings, as illustrated in Fig. 10. At the center of these vortex rings, the vertical velocity reaches its maximum value, between about 100 and 120 $\text{m} \cdot \text{s}^{-1}$. The effective measurement instant $\tilde{\Delta}t_{\text{jet}}$ is very close to the instant extracted from the simulation t_{LES}.

The comparison of the two velocity fields shows that the model correctly reproduces the position of the leading vortex ring at $y \simeq 2.3$ mm. The high velocity values are also satisfactorily reproduced, with a difference of about 20% at most on the maximal vertical velocity. In the simulation, two secondary vortex rings following the leading one are observed. They are clearly visible on the horizontal velocity field, their centers being located approximately at $y \simeq 1$ mm and $y \simeq 0.4$ mm. Interestingly, only one secondary vortex ring can be identified on the PIV measurements, at $y \simeq 0.5$ mm. This is actually because of the merging of the other vortex ring with the leading one at this instant in the experiment, as revealed by the particle images (see Fig. 11a). After some tests, this slight difference observed between the simulation and the experiment is assumed to originate from a small difference in the actuator geometry between the model and the real actuator. Nevertheless, similar comparisons between experimental and numerical results at other instants of the jet development prove that the main jet dynamics are correctly reproduced by the simulation. Because the LES model is able to reproduce the main features of the jet, such as the development of the leading vortex and the generation of secondary vortices, it can be used to investigate in a significant manner the sources of uncertainty and the particle dynamics errors that were not accessible with the measurements.

C. Velocity Uncertainty Related to the Laser Sheet Position

Relying on this model, an evaluation of the significance of the velocity uncertainty yielded by the position uncertainty of the laser sheet can be performed using the numerical PIV-like images. In the experiment, the laser sheet position is estimated to be $r = 0.25 \pm 0.1$ mm, as indicated in Sec. I. Considering a rectangular distribution, the standard uncertainty of the laser sheet position is $(0.1/\sqrt{3})$mm. Thereby, the standard velocity uncertainty due to the uncertainty of the laser sheet position is given by

$$u_r(\boldsymbol{m}) = \frac{\partial \bar{V}(\boldsymbol{m})}{\partial r} \frac{0.1}{\sqrt{3}} \tag{7}$$

where $\partial \bar{V}(\boldsymbol{m})/\partial r$ is the partial derivative of the phase-averaged velocity with respect to the laser sheet position r. This term is deduced from the simulation and relies on the PIV-like process applied on two numerical laser sheets, extracted at $r = 0.15$ and 0.35 mm to estimate $\partial \bar{V}(\boldsymbol{m})/\partial r$ using a second-order central finite difference scheme. The resulting velocity uncertainty field relative to the maximum velocity V_{max} is displayed on Fig. 12 for the instant $t_{\text{LES}} = 94\ \mu$s. Comparing the orders of magnitude with those

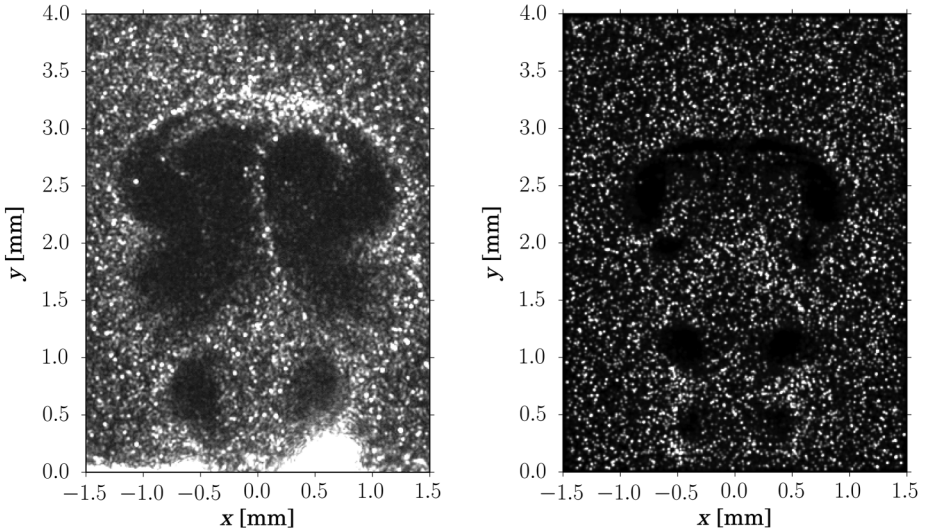

a) An example of experimental particle image at $\Delta\tilde{t}_{jet} = 94.6$ μs; the brightness is artificially increased for the sake of clarity

b) An example of numerical particle image obtained following the methodology presented in Sec. IV using the LES and the Lagrangian solver with different classes of particles at $t_{LES} = 94$ μs

Fig. 11 Comparison of experimental and numerical particle images.

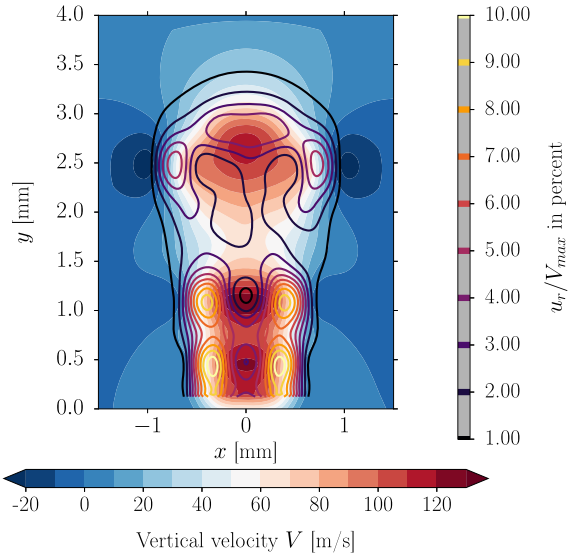

Fig. 12 Vertical velocity field V obtained by LES at the instant $t_{\mathrm{LES}} = 94$ μs overlaid with isolines of relative velocity uncertainty u_r/V_{max} yielded by the numerical laser sheet positions reproducing the experimental position uncertainty.

obtained for Figs. 8a and 8b, it appears that the laser sheet position can be the major source of uncertainty for this type of experiment. As expected, the regions of highest uncertainty coincide with the locations of vortical structures. Typically, one can see that relative velocity uncertainties induced by the laser sheet position can be as high as 10% in some regions of the jet, corresponding to areas where velocity gradients are the highest, near the actuator orifice. Regarding the leading vortex at the instant considered, relative uncertainties ranging from 3 to 5% can be typically expected, which are then dominating the ones estimated in Sec. II.D.

Because of the slight topology discrepancies observed between the PIV measurements and the simulation in some regions of the jet, it may not be advisable to combine these numerical results with the experimental ones through a propagation of uncertainties to provide global uncertainty estimates of the PIV measurements. It is nonetheless argued that the present simulation, although not being perfect, provides a representation of the flowfield that is in sufficient adequacy with the flow topology measured to quantitatively conclude on the importance of the source of uncertainty here investigated. It is thus stated that, for such high-speed vortical flows, this source of uncertainty plays a major role and should be carefully addressed while considering such planar PIV measurements.

IV. Particle Dynamics Study

The numerical model is now employed to study the seeding particle dynamics, with the objective to investigate the potential PIV measurement errors originating from the slip velocities between these particles and the gaseous flowfield. Indeed, as detailed in the Introduction, usual assumptions made for PIV measurements may not be verified for such transient high-speed flows.

First, particle trajectories are computed on the basis of the LES model presented in Sec. III using a Lagrangian dispersed phase solver. The experimental particle size distribution is approximated using several distinct classes. Numerical particle images are then generated from the two-phase flow simulation, each image pair being computed with a different initial spatial particle distribution. Velocity fields are then calculated from these images using the PIV algorithm. The resulting averaged velocity field is intended to be practically independent of the initial spatial particle distribution. Finally, this field is compared with the gaseous reference velocity field to determine the influence of particle dynamics on the PIV results.

A. Two-Phase Flow Simulation

The LES model of the PSJ actuator presented in Sec. III is coupled with a Lagrangian solver for the dispersed phase. This solver is also integrated in the ONERA in-house CFD platform CEDRE. In the experiment, the particle concentration is roughly estimated as 3×10^{13} particles/m^3, based on the analysis of the particle images made in the next section. Accounting for the entire particle size distribution shown in Fig. 2c, the volume fraction of particles in the gas is about 2×10^{-7}, whereas the particles are separated on average by a distance of about 32 μm. These values are sufficiently low to assume that the coupling between the gas phase and the particle phase is only one way [34]: The gas phase influences the particle trajectories, but the particles do not alter the gas phase in return. Moreover, particle interactions are negligible due to the large

innerparticle distance. Thus, the velocity field of the gas phase is unaltered by the presence of the particles.

In the PIV experiment, the density ratio between the particle phase and the gas phase is about 760. In conjunction with the very small particle diameters encountered in the present experiment, such a high density ratio implies that the drag force largely exceeds any other force applied to the particles [17,18]. The particle Reynolds number, defined by

$$Re_p = \frac{\rho_g d_p \|\boldsymbol{V}_p - \boldsymbol{V}_g\|}{\mu_g} \tag{8}$$

does not exceed eight in the experiment. This maximum value is obtained using the largest particle diameter and assuming a slip velocity $\|\boldsymbol{V}_p - \boldsymbol{V}_g\| = V_{\max}$. The drag coefficient may thus be computed with Schiller and Naumann's correlation [35], which remains valid until approximately $Re_p < 800$ [36].

An unconditionally stable first-order time stepping scheme is used to integrate the particle trajectories [37]. Given the very small time step value considered in the present simulation (i.e., $\delta t = 10^{-9}$ s), the resulting accuracy of this scheme is fully acceptable. The gas-phase properties are interpolated at the particle locations using the gradients provided by the Navier–Stokes solver, yielding a second-order spatial accuracy. The Haselbacher et al. [38] algorithm is used to localize particles on the grid.

Seven particle classes are computed. This choice is the result of a compromise between a fine description of the particle size distribution (Fig. 2c) and a limited computational cost. Each class represents a particular range of diameters in the particle size distribution. In the numerical simulation, the diameters attributed to each class correspond to the mean of each size interval, as reported in Table 1.

The particles are initialized with vanishing velocity and placed inside a box above the actuator orifice, defined by a square cylinder with a base of 3×3 mm and a height of 8 mm. With these dimensions, the box contains all particles able to move in the region of interest, that is, the laser sheet viewed by the camera. In addition, some particles are placed inside the nozzle part of the actuator cavity.

A distinct numerical simulation could have been performed to compute particle trajectories for every initial spatial distribution. However, this would have involved a significant computational cost. Because the coupling is only one way, particle trajectories are independent of each other, and only one simulation displaying an initial particle concentration much higher than in the experiment is conducted. Using appropriate postprocessing steps, trajectories of any initial spatial distribution and any particle size distribution may be extracted, as will be detailed in the next sections.

B. Results Analysis

Before creating the particle images, the particle dynamics are characterized for each class separately. Here, the particle trajectories extracted through postprocessing are obtained from an almost homogeneous and dense initial spatial distribution. The particles are located in a slice representative of the experimental laser sheet. The representative instant $t_{\text{LES}} = 94$ μs is chosen for postprocessing.

Table 1 Particle classes characteristics

Range of real diameters, μm	Class diameter, μm	Class stokes number	Class normalized intensity	Class occurrence probability
[0.14; 0.18]	0.16	0.029	1.25×10^{-4}	0.2254
[0.18; 0.22]	0.20	0.045	1.27×10^{-3}	0.3713
[0.22; 0.26]	0.24	0.065	9.72×10^{-3}	0.2520
[0.26; 0.30]	0.28	0.088	5.74×10^{-2}	0.0921
[0.30; 0.40]	0.35	0.138	4.63×10^{-1}	0.0385
[0.40; 0.50]	0.45	0.228	8.49×10^{-1}	0.0125
[0.50; 0.60]	0.55	0.341	1.0	0.0083

Figure 13 represents the concentration fields for each numerical particle class per interrogation window. The concentration is normalized by its maximum value for each class. As in the FOLKI-SPIV software, an interrogation window is computed around each pixel. For the sake of clarity, the PIV-like processed vorticity of the gas phase is also reported. In Fig. 13b, all particle trajectories are considered, whereas in Fig. 13a, the trajectories of particles originating from the cavity at the initial instant have been discarded. First, these figures demonstrate that, if particles are initially absent from the cavity, the particle concentration remains very low in the lower part of the jet core. Observing the particle images in Figs. 6 and 11, it appears that the particle concentrations in this zone are similar to those observed outside the jet. Given these results, it can be reasonably assumed that some particles are actually originating from the cavity. Consequently, the following analysis only considers the results obtained in this case.

Despite the fact that some particles may have been exposed to a strong electrical field during the discharges, electrical forces are assumed negligible with respect to the drag force. The main reason is that the electrical field vanishes about 10 μs before the beginning of the ejection phase. The particle relaxation time τ_p introduced in Sec. I is estimated at a maximum value of 1 μs. It is thus reasonable to assume that particles are at dynamic equilibrium with the gas (i.e., that they have vanishing velocities at the beginning of the ejection phase). Thus, electrical forces should have no influence on the velocity measurement.

Figure 13b shows that all particle classes display a significantly lower concentration in high-vorticity areas. This confirms the interaction dynamics between particles and vortex rings discussed in Sec. II.C (i.e., the low probability for particles to stay within vortex rings, even for those with a very low Stokes number of about 0.029). As expected, the particle concentration in high-vorticity zones decreases as the class diameter increases.

The velocity field of each particle class is shown in Fig. 14a. To obtain these fields, a processing similar to the PIV-like process is performed (see Sec. III). Relying on the previous analysis, the particles located in each interrogation window are identified. For each interrogation window, the mean velocity is calculated through a weighted average of these particle velocities. The weights follow the Gaussian distribution of the light intensity within the laser sheet. In the following, the velocity fields obtained with this process will be referred to as the *velocity fields of particles*. With such a process, if particles perfectly follow the gas phase in each point, and if the particle concentration is infinite and homogeneous in each interrogation window, the velocity field of particles should be equal to the velocity field of the gas phase yielded by the PIV-like process (barring interpolation errors inherent to this one). Figure 14b illustrates the velocity differences between these two fields, relative to the maximal velocity of the gas phase (i.e., 125 m/s). In Fig. 14b, the first column of images shows the reference vorticity field obtained by LES for comparison purpose, depicting the location of the vortex rings. As expected, the differences are closely linked to the vorticity value and they increase with the particle diameter. The maximal differences are about 20% for the $d = 0.16$ μm class and about 40% for the $d = 0.55$ μm class. Such high values are reached because of slip velocities, but also because of differences in particle concentrations between high-vorticity zones and external zones. Indeed, when an interrogation window contains two such zones, the averaged particle velocity gets closer to the particle velocities found in the external zones, where the particle concentration is higher, than it would be in a perfectly homogeneous case. Table 2 gives the maximal value of the vertical slip velocity for each particle class, relative to the maximal vertical velocity of the gas phase. These values are computed in the vicinity of the median plane of the laser sheet. They indicate that the concentration ratio is the main reason of the differences observed in Fig. 14b.

This analysis does not yield an estimate of the possible error that should be expected in the experiment, but rather a first estimate of the impact of particle dynamics on differences between the particle velocity fields and the gas-phase velocity fields. To investigate the potential error induced by the particle dynamics on the PIV

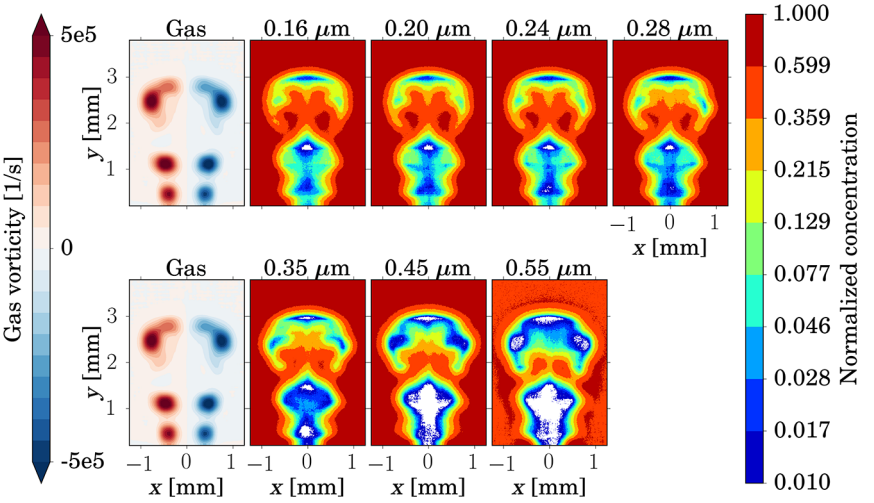

a) Numerical particle concentration fields evaluated by discarding particles coming from the actuator cavity (white areas correspond to normalized concentration inferior to 10^{-3})

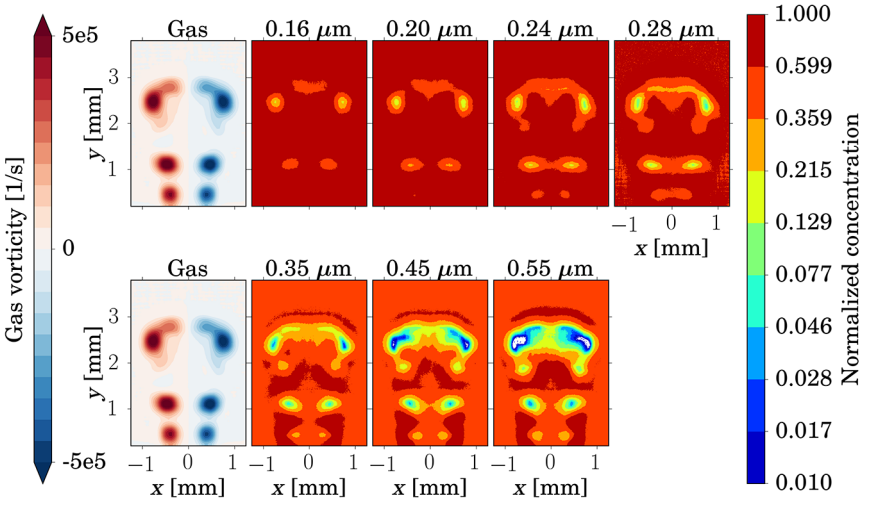

b) Numerical particle concentration fields evaluated by including particles coming from the actuator cavity

Fig. 13 Contour map of the gas phase vorticity obtained by LES (first column of images, the same map is duplicated for clarity and comparison purpose with maps along each row) together with the contour maps of the normalized particle concentration for each particle class whose diameter is indicated on the top of the each figure; results obtained at the instant $t_{\mathrm{LES}} = 94$ μs a) without and b) with particles in the actuator cavity.

measurement, the final step is to consider the effect of light diffusion. Indeed, particle classes are mixed in PIV experiments, resulting in a competition for the PIV results between light diffusion (higher for the largest particles) and particle concentration (higher for the smallest particles). The next sections tackle this aspect through the creation of particle images.

C. Particle Image Creation

In this section, the process leading to the generation of realistic numerical particle image pairs is described. As explained earlier, the two-phase flow simulation computes the trajectories of many more particles than in the experimental case. Given an appropriate selection mechanism, many uncorrelated particle seeding fields with a concentration matching the experiment may thus be defined in the numerical simulation. Each of these initial numerical particle fields results in distinct particle image pairs for a given computational instant. The velocity fields deduced from them may then be averaged to obtain numerical results that are almost independent from the initial spatial distribution of particles.

The particle selection process implies the random generation of particle sets with a spatially homogeneous distribution. Furthermore, each set should approximately satisfy the experimental size distribution. Therefore, the probability of selecting a particle with a diameter d and initially placed in a cell with a volume $\mathcal{V}_{\mathrm{cell}}$ is written as

$$P = C\mathcal{V}_{\mathrm{cell}}F(d) \tag{9}$$

where C is the global concentration of particles at the initial instant and $F(d)$ is the occurrence probability of the class diameter d. Weighing the size distribution by the cell volume and the estimated particle concentration allows one to compensate concentration inhomogeneities arising from the numerical seeding procedure, which consists of placing a constant number of particles in each computational cell. The values used for the discrete particle size distribution $F(d)$ are reported in Table 1. In this study, 100 different numerical initial seeding fields are generated, allowing one to compute as many particle image pairs for any desired computational time step.

To create a particle image, the footprint of each selected particle on the synthetic image has to be calculated. Raffel et al. [39] express the particle image diameter as

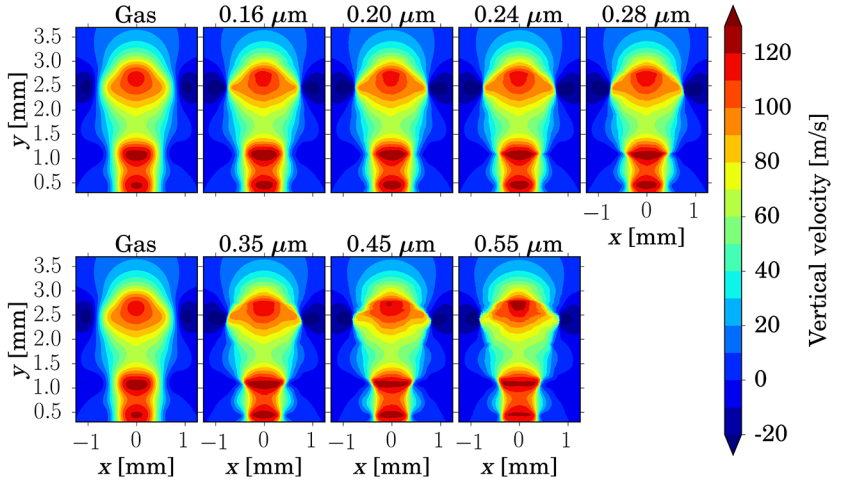

a) Vertical velocity fields

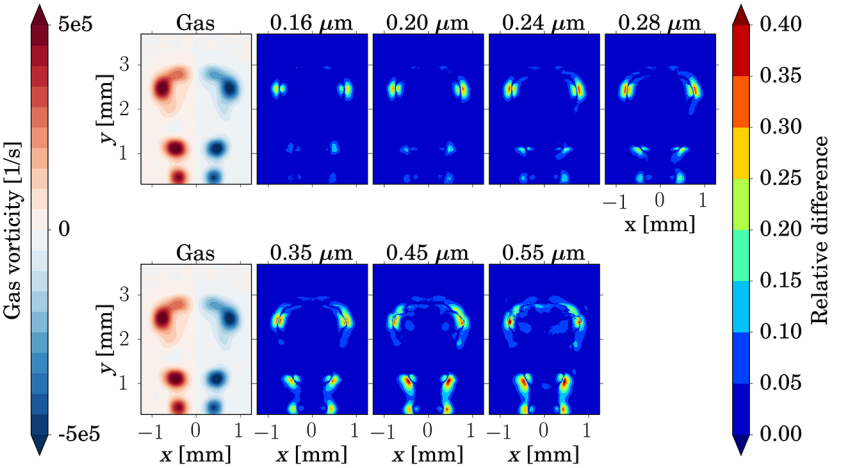

b) Absolute differences of vertical velocity fields relative to the maximal gas velocity

Fig. 14 Vertical velocity fields and differences for each class of particles. a) vertical velocity fields V obtained by LES for the gas phase, providing the reference field in the first column of figures, and obtained by considering the various classes of particles as detailed in Sec. IV at the instant $t_{\mathrm{LES}} = 94\ \mu$s; b) Absolute differences obtained between the particle velocity fields provided in Fig. 14a and the reference field of vertical velocity yielded by LES, relative to the maximum velocity V_{max}.

$$d_\tau = \sqrt{(Md_p)^2 + d_d^2} \tag{10}$$

where M is the magnification factor of the lens and d_d is the diffraction limited minimum image diameter. In the present PIV experiment, d_τ covers about 4 pixels, that is 28 μm, whereas Md_p is inferior to 0.7 μm. Thus, the particle image diameter is largely dominated by diffraction, which is the only phenomenon taken into account in the following. The intensity pattern created by a particle on an image, theoretically described by the Airy function, is approximated by a Gaussian function, as suggested by Raffel et al. [39]. The width is fixed to a constant value to reproduce the value of d_τ observed in the experiment. To calculate the intensity amplitude given by the light scattering of the particle, a strong assumption is made: Every particle is considered isolated from the others. This considerably simplifies the calculation, because, with this hypothesis, the incident light on a given particle only originates from the laser sheet. In other words, the light scattered by the other particles in the laser sheet to this given particle is not taken into account. Because the light scattering globally increases with the particle diameter, with this assumption, the computed velocity fields are more sensitive to the large particles than in the experimental case. The present study thus provides an upper bound of the error. The scattered light is evaluated for each particle class, with the Lorenz–Mie theory, considering the polarization of the laser sheet. The DELPI software [40,41] is used for this calculation. The light intensity is integrated over the scattering angles seen by the camera lens, roughly between 89.1 and 90 deg, and over the range of diameters represented by each class. The normalized results are given in Table 1. The final intensity amplitudes used for the particle image creation are obtained by multiplying these values by the normalized value of the laser sheet intensity, which has a Gaussian profile, at the particle position. Finally, the synthetic images are obtained by the superposition of the footprints of all particles. For each particle image pair, the second image is deduced from the first one, knowing the velocity of the particles and the time delay between the two laser pulses.

Table 2 Maximal slip vertical velocity of particles relative to the maximal vertical velocity of the gas phase

Characteristics	Classes of particles						
Diameter, μm	0.16	0.20	0.24	0.28	0.35	0.45	0.55
Slip velocity, %	6.1	6.1	6.2	6.2	7.3	9.3	12

Figure 11 shows an example of numerical particle image resulting from the aforementioned processing steps. It is compared with an experimental particle image captured at the same instant of the jet development. Several calculations of numerical particle images were performed with different initial global concentration levels C. The value $C = 3 \times 10^{13}$ particles/m^3 was used in the presented figure

because it yielded the best agreement with experiments. The topology of the particle concentration in the jet is globally well reproduced in the numerical image. Nonetheless, some differences can be noticed. As discussed in Sec. III, the second vortex ring starts to merge earlier with the leading vortex ring in the experiment than in the simulation. This effect probably explains why the area of low particle concentration appears slightly larger in the experiments. Nevertheless, the particle concentration in the leading vortex ring appears slightly lower in the experimental image than in the numerical one. This could be explained by different particle concentrations in the cavity at the initial instant between experiment and numerical simulation. Indeed, due to lack of quantitative experimental data, the particle concentrations were assumed identical in the seeding box and the cavity for the numerical simulation. Finally, a background noise is visible on the experimental image, but it was not computed in the numerical images.

Because the numerical particle images successfully reproduce the main flow features observed in the experimental images, they may now be used to investigate the possible experimental errors. Similar to the uncertainty estimation performed in Sec. III.C, it is acknowledged that the reliability of the results then obtained are limited by the quality of the numerical model. It is, however, argued that the present model should be sufficiently representative to provide reliable orders of magnitudes of such errors.

D. Estimation of Errors due to the Particle Dynamics

The velocity fields are retrieved from the numerical particle images in the same manner as the experimental particle images. An average over 100 velocity fields is then performed. This number seems sufficient to obtain statistically converged results for the mean. Furthermore, the independence of the present results on the initial spatial particle distribution was verified.

Figure 15 illustrates the results obtained at the instant $t_{\mathrm{LES}} = 94\ \mu$s, which was previously identified as representative of the jet dynamics. The PIV-like processed vertical velocity of the gas phase is displayed on the right. Isolines of errors on vertical velocity with respect to the maximum gas-phase vertical velocity at the same instant are overlayed on the same figure. The left part of the figure illustrates the vorticity of the gas phase, calculated from the PIV-like processed velocity fields, highlighting the location of the centers of the vortex rings. In a large part of the jet, the errors lie below 5%. In the center of the vortex rings, the calculated error is higher than 10%, locally reaching a value of about 25% for the leading vortex ring and 30% for the secondary one. In fact, the relative errors obtained from particle images are close to the ones obtained for the class $d = 0.35\ \mu$m (see Fig. 14b). It thus seems that this class offers the best compromise between light diffusion and initial concentration.

To conclude this particle dynamics study, two results are highlighted. First, the velocity fields measured with the PIV technique appear to coincide with the velocity of particles that have a diameter larger than the mean of the present particle size distribution. Second, according to the numerical results, significant velocity measurement errors are likely to particularly arise in the vicinity of the vortex rings. Velocity slip is partly responsible, but the main reason is found in the concentration differences between the vortex ring cores and the rest of the flow. The results obtained in such zones have then to be carefully considered because errors may amount to 25–30%.

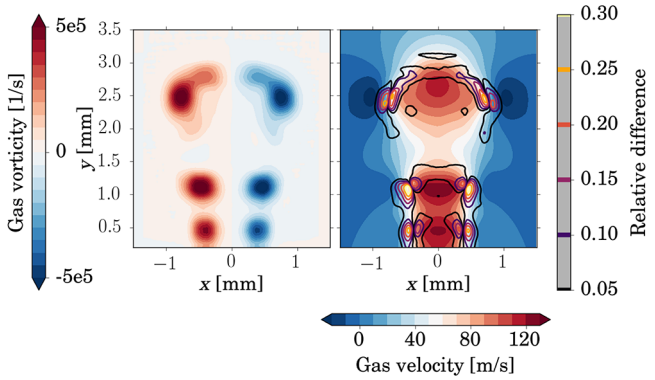

Fig. 15 PIV-like processed numerical fields yielded by LES at the instant $t_{\mathrm{LES}} = 94\ \mu$s: (left) gas vorticity; (right) vertical velocity overlaid with isolines of errors relative to the maximum velocity of the gas phase $V_{\max}$ at the same instant.

V. Conclusions

In the present article, a planar particle image velocimetry (PIV) measurement of the jet generated by a plasma synthetic jet actuator was analyzed with a particular focus on two points: the measurement uncertainty associated with such an experiment conducted on a millimeter-scale high-speed transient flow and the measurement errors due to the particle dynamics.

The uncertainty analysis focused on three different sources that were considered predominant for this type of experiment: the statistical uncertainty of the phase-averaging process, the uncertainty of the wall position on the particle images, and the uncertainty of the laser sheet position. Although the contribution of the first two sources could be directly deduced from the measurements, the significance of the contribution of the laser sheet position uncertainty was discussed based on an large-eddy simulation model. Although perfectible, the numerical model was shown to produce a satisfactory representation of the vortex dynamics compared with the experiments, allowing one to rely on its results to investigate this last source of uncertainty. Based on an estimation of the laser sheet position uncertainty, this analysis supports in a quantitative manner its prominent role in the evaluation of global uncertainty estimates, because it appears to dominate the other sources of uncertainty where large velocity gradients are observed. Typical values of relative velocity uncertainty ranging from 4 to 8% were observed in regions of the jet where vortical structures develop.

This numerical model coupled with a Lagrangian dispersed phase solver was then also employed to investigate the possible measurement errors associated with nonideal particle dynamics. The experimental particle size distribution was represented using seven particle classes, each of them being postprocessed separately. As expected, high-vorticity areas displayed much lower particle concentrations than other parts of the jet, even for particles with very low Stokes number, and the concentration ratio decreased as the Stokes number increased. Furthermore, accounting for interrogation windows to evaluate the velocity fields in a PIV manner induced significant velocity differences in the regions of high vorticity between the particles and the gas phase. It was concluded that these discrepancies are mainly the result of particle concentration differences between high- and low-vorticity areas rather than slip velocities between particles and gas.

Finally, an estimation of the velocity errors to be expected in the PIV experiment was realized through the generation of realistic synthetic particle images. The light intensity scattered by the particles was computed according to the Lorenz–Mie theory. Each image pair corresponds to a different initial spatial particle distribution. The 100 image pairs generated were processed in a similar manner as the experimental PIV images. The resulting averaged velocity fields appeared almost independent from the initial spatial particle distribution. It was observed that the particle class that yielded the best agreement with experimental results was neither the most concentrated one, nor the one that scattered the highest light intensity, but a compromise between the two. At last, the averaged velocity field calculated from particle images was compared with the velocity of the gaseous phase processed to account for the interrogation window size and the laser sheet width. The resulting velocity differences provided an estimate of the velocity errors that could be expected for such PIV measurements. The velocity errors highlighted are particularly significant in the vicinity of vortex ring cores, with relative values typically as high as 25–30%. These results thus suggest that, for this type of transient high-speed vortical flows, the sole consideration of a

standard global Stokes number cannot suffice to guarantee low PIV measurement errors.

Although largely depending on the quality of the numerical flow model, this methodology can usefully supplement PIV measurements, allowing one, as in the present study, to investigate uncertainties and errors that can be hardly accessible through experiments.

Acknowledgments

This work received financial support from the Direction Générale de l'Armement and from ONERA—The French Aerospace Lab. The authors thank Yves Le-Sant for his assistance in the optical calibration and in the usage of FOLKI-SPIV.

References

[1] Cattafesta, L. N., and Sheplak, M., "Actuators for Active Flow Control," *Annual Review of Fluid Mechanics*, Vol. 43, No. 1, 2011, pp. 247–272. doi:10.1146/annurev-fluid-122109-160634

[2] Glezer, A., "Some Aspects of Aerodynamic Flow Control Using Synthetic-Jet Actuation," *Philosophical Transactions of the Royal Society of London, Series A: Mathematical and Physical Sciences*, Vol. 369, No. 1940, 2011, pp. 1476–1494. doi:10.1098/rsta.2010.0374

[3] Glezer, A., and Amitay, M., "Synthetic Jets," *Annual Review of Fluid Mechanics*, Vol. 34, No. 1, 2002, pp. 503–529. doi:10.1146/annurev.fluid.34.090501.094913

[4] Grossman, K., Cybyk, B., and VanWie, D., "Sparkjet Actuator for Flow Control," *41st Aerospace Sciences Meeting and Exhibit*, AIAA Paper 2003-0057, 2003. doi:10.2514/6.2003-57

[5] Hardy, P., Barricau, P., Belinger, A., Caruana, D., Cambronne, J., and Gleyzes, C., "Plasma Synthetic Jet for Flow Control," *40th Fluid Dynamics Conference and Exhibit*, AIAA Paper 2010-5103, 2010. doi:10.2514/6.2010-5103

[6] Chedevergne, F., Léon, O., Bodoc, V., and Caruana, D., "Experimental and Numerical Response of a High-Reynolds-Number $M = 0.6$ Jet to a Plasma Synthetic Jet Actuator," *International Journal of Heat and Fluid Flow*, Vol. 56, 2015, pp. 1–15. doi:10.1016/j.ijheatfluidflow.2015.06.008

[7] Caruana, D., Cambronne, J.-P., Barricau, P., and Belinger, A., "The Plasma Synthetic Jet Actuator for Separation Control," *Ercoftac Series*, Vol. 94, 2013, pp. 17–22.

[8] Caruana, D., Barricau, P., and Gleyzes, C., "Separation Control with Plasma Synthetic Jet Actuators," *International Journal of Aerodynamics*, Vol. 3, Nos. 1–3, 2013, pp. 71–83. doi:10.1504/IJAD.2013.050925

[9] Molton, P., Leroy-Chesneau, A., Pons, J., Carpels, Y., Barricau, P., Gleyzes, C., Forte, M., and Caruana, D., "Wing Tip Vortex Control by Plasma Actuators," *Ercoftac Series*, Vol. 94, 2013, pp. 53–58.

[10] Narayanaswamy, V., Raja, L. L., and Clemens, N. T., "Control of Unsteadiness of a Shock Wave/Turbulent Boundary Layer Interaction by Using a Pulsed-Plasma-Jet Actuator," *Physics of Fluids*, Vol. 24, No. 7, 2012, Paper 076101. doi:10.1063/1.4731292

[11] Reedy, T. M., Kale, N. V., Dutton, J. C., and Elliot, G. S., "Experimental Characterization of a Pulsed Plasma Jet," *AIAA Journal*, Vol. 51, No. 8, 2013, pp. 2027–2031. doi:10.2514/1.J052022

[12] Ko, H., Haack, S., Land, H., Cybyk, B., Katz, J., and Kim, H., "Analysis of Flow Distribution from High-Speed Flow Actuator Using Particle Image Velocimetry and Digital Speckle Tomography," *Flow Measurement and Instrumentation*, Vol. 21, No. 4, 2010, pp. 443–453. doi:10.1016/j.flowmeasinst.2010.06.001

[13] Cybyk, B., Simon, D., Land, H., III, Chen, J., and Katz, J., "Experimental Characterization of a Supersonic Flow Control Actuator," *44th AIAA Aerospace Sciences Meeting and Exhibit*, AIAA Paper 2006-0478, 2006. doi:10.2514/6.2006-478

[14] Sciacchitano, A., Neil, D. R., Smith, B. L., Warner, S. O., Vlachos, P. P., Wieneke, B., and Scarano, F., "Collaborative Framework for PIV Uncertainty Quantification: Comparative Assessment of Methods," *Measurement Science and Technology*, Vol. 26, No. 7, 2015, Paper 074004. doi:10.1088/0957-0233/26/7/074004

[15] Lazar, E., DeBlauw, B., Glumac, N., Dutton, C., and Elliott, G., "A Practical Approach to PIV Uncertainty Analysis," *27th AIAA Aerodynamic Measurement Technology and Ground Testing Conference*, AIAA Paper 2010-4355, 2010.

[16] Zong, H., and Kotsonis, M., "Effect of Slotted Exit Orifice on Performance of Plasma Synthetic Jet Actuator," *Experiments in Fluids*, Vol. 58, No. 3, 2017, p. 17. doi:10.1007/s00348-016-2299-1

[17] Maxey, M. R., and Riley, J. J., "Equation of Motion for a Small Rigid Sphere in a Nonuniform Flow," *Physics of Fluids*, Vol. 26, No. 4, 1983, pp. 883–889. doi:10.1063/1.864230

[18] Melling, A., "Tracer Particles and Seeding for Particle Image Velocimetry," *Measurement Science and Technology*, Vol. 8, No. 12, 1997, pp. 1406–1416. doi:10.1088/0957-0233/8/12/005

[19] Adrian, R. J., and Westerweel, J., *Particle Image Velocimetry*, Cambridge Univ. Press, New York, 2011, , pp. 40–71, Chap. 2.

[20] Reedy, T. M., Kale, N. V., Dutton, J. C., and Elliot, G. S., "Experimental Characterization of a Pulsed Plasma Jet," *50th AIAA Aerospace Science Meeting Including the New Horizons Forum and Aerospace Exposition*, AIAA Paper 2012-0904, 2012. doi:10.2514/6.2012-904

[21] Samimy, M., and Lele, S. K., "Motion of Particles with Inertia in a Compressible Free Shear Layer," *Physics of Fluids*, Vol. 3, No. 8, 1991, pp. 1915–1923. doi:10.1063/1.857921

[22] Williams, O. J. H., Nguyen, T., Schreyer, A.-M., and Smits, A. J., "Particle Response Analysis for Particle Image Velocimetry in Supersonic Flows," *Physics of Fluids*, Vol. 27, No. 7, 2015, Paper 076101. doi:10.1063/1.4922865

[23] Mitchell, D., Honnery, D., and Soria, J., "Particle Relaxation and Its Influence on the Particle Image Velocimetry Cross-Correlation Function," *Experiments in Fluids*, Vol. 51, No. 4, 2011, pp. 933–947. doi:10.1007/s00348-011-1116-0

[24] De Silva, C. M., Baidya, R., Khashehchi, M., and Marusic, I., "Assessment of a Tomographic PIV in Wall-Bounded Turbulence Using Direct Numerical Simulation Data," *Experiments in Fluids*, Vol. 52, No. 2, 2012, pp. 425–440. doi:10.1007/s00348-011-1227-7

[25] Bera, J. C., Michard, M., Grosjean, N., and Comte-Bellot, G., "Flow Analysis of Two-Dimensional Pulsed Jets by Particle Image Velocimetry," *Experiments in Fluids*, Vol. 31, No. 5, 2001, pp. 519–532. doi:10.1007/s0034801003141

[26] Lawson, J., and Dawson, J., "The Formation of Turbulent Vortex Rings by Synthetic Jets," *Physics of Fluids*, Vol. 25, No. 10, 2013, Paper 105113. doi:10.1063/1.4825283

[27] Amitay, M., and Cannelle, F., "Evolution of Finite Span Synthetic Jets," *Physics of Fluids*, Vol. 18, No. 5, 2006, Paper 054101. doi:10.1063/1.2196093

[28] Laurendeau, F., Chedevergne, F., and Casalis, G., "Transient Ejection Phase Modeling of a Plasma Synthetic Jet," *Physics of Fluids*, Vol. 26, No. 12, 2014, Paper 125101. doi:10.1063/1.4902394

[29] Belinger, A., Hardy, P., Barricau, P., Cambronne, J., and Caruana, D., "Influence of the Energy Dissipation Rate in the Discharge of a Plasma Synthetic Jet Actuator," *Journal of Physics D: Applied Physics*, Vol. 44, No. 36, 2011, Paper 365201. doi:10.1088/0022-3727/44/36/365201

[30] Greason, W. D., "Methodology to Study the Resistance of a Spark Discharges," *IEEE Transactions on Industry Applications*, Vol. 35, No. 2, March/April 1999, pp. 359–365. doi:10.1109/28.753629

[31] Belinger, A., Naudé, N., Cambronne, J.-P., and Caruana, D., "Plasma Synthetic Jet Actuator: Electrical and Optical Analysis of the Discharge," *Journal of Physics D: Applied Physics*, Vol. 47, No. 34, 2014, Paper 345202. doi:10.1088/0022-3727/47/34/345202

[32] Champagnat, F., Plyer, A., Le Besnerais, G., Leclaire, B., Davoust, S., and Le Sant, Y., "Fast and Accurate PIV Computation Using Highly Parallel Iterative Correlation Maximization," *Experiments in Fluids*, Vol. 50, No. 4, 2011, pp. 1169–1182. doi:10.1007/s00348-011-1054-x

[33] "EA-4/02 Expression of the Uncertainty of Measurement in Calibration," *European Co-Operation for Accreditation*, Paper EA 4/02, Paris, France, 1999, pp. 1–79.

[34] Alletto, M., and Breuer, M., "One-Way, Two-Way and Four-Way Coupled LES Predictions of a Particle-Laden Turbulent Flow at High

Mass Loading Downstream of a Confined Bluff Body," *International Journal of Multiphase Flow*, Vol. 45, 2012, pp. 70–90. doi:10.1016/j.ijmultiphaseflow.2012.05.005

[35] Schiller, L., and Naumann, A., "A Drag Coefficient Correlation," *Vdi Zeitung*, Vol. 77, No. 318, 1935, p. 51.

[36] Crowe, C. T., *Multiphase Flow Handbook*, CRC Press, Boca Raton, 2005, pp. 1–79, Chap. 1.

[37] Murrone, A., and Villedieu, P., "Numerical Modeling of Dispersed Two-Phase Flows," *AerospaceLab* [online journal], Vol. 4, No. 2, March 2011, pp. 1–13, http://www.aerospacelab-journal.org/.

[38] Haselbacher, A., Najjar, F. M., and Ferry, J. P., "An Efficient and Robust Particle-Localization Algorithm for Unstructured Grids," *Journal of Computational Physics*, Vol. 225, No. 2, 2007, pp. 2198–2213. doi:10.1016/j.jcp.2007.03.018

[39] Raffel, M., Willert, C. E., Wereley, S. T., and Kompenhans, J., *Particle Image Velocimetry*, 2nd ed., Springer-Verlag, New York, 1998, pp. 15–79, Chap. 2.

[40] Onofri, F., Gréhan, G., and Gouesbet, G., "Electromagnetic Scattering from a Multilayered Sphere Located in an Arbitrary Beam," *Applied Optics*, Vol. 34, No. 30, 1995, pp. 7113–7124. doi:10.1364/AO.34.007113

[41] Onofri, F., Lenoble, A., Radev, S., and Guering, P.-H., "High Resolution Monitoring of an Unsteady Glass Fibre Drawing Process," *Experiments in Fluids*, Vol. 42, No. 4, 2007, pp. 601–610. doi:10.1007/s00348-007-0268-4

A. Naguib
Associate Editor